

SCIENTIFIC REPORTS

OPEN

Structural, luminescence and thermometric properties of nanocrystalline $\text{YVO}_4:\text{Dy}^{3+}$ temperature and concentration series

I. E. Kolesnikov^{1,2}, A. A. Kalinichev¹, M. A. Kurochkin¹, E. V. Golyeva^{3,4}, A. S. Terentyeva³, E. Yu. Kolesnikov⁵ & E. Lähderanta²

We report systematic study of Dy^{3+} -doped YVO_4 nanophosphors synthesized via modified Pechini technique. Effect of calcination temperature and doping concentration on structure and luminescence has been investigated. XRD and Raman spectroscopy revealed preparation of single phase nanoparticles without any impurities. Synthesized nanopowders consisted of weakly agglomerated nanoparticles with average size about 50 nm. Photoluminescence spectra of $\text{YVO}_4:\text{Dy}^{3+}$ nanoparticles consisted of the characteristic narrow lines attributed to the intra-configurational 4f-4f transitions dominating by the hypersensitive ${}^4\text{F}_{9/2}-{}^6\text{H}_{13/2}$ transition. The calcination temperature variation did not affect ${}^4\text{F}_{9/2}$ lifetime, whereas increase of doping concentration resulted in its gradual decline. Potential application of $\text{YVO}_4:\text{Dy}^{3+}$ 1 at.% and 2 at.% nanopowders as ratiometric luminescence thermometers within 298–673 K temperature range was tested. The main performances of thermometer including absolute and relative thermal sensitivities and temperature uncertainty were calculated. The maximum relative thermal sensitivity was determined to be $1.8\% \text{ K}^{-1}$ @ 298 K, whereas the minimum temperature uncertainty was 2 K.

In last decades rare earth materials have been widely used as high-performance luminescent devices, catalysts, and other functional materials based on the electronic, optical, and chemical characteristics arising from their 4f electrons^{1–5}. The unique 4f electronic configuration of rare earth elements makes them perfect phosphors emitting light ranging from UV to NIR. Hence, rare earth doped materials are potential candidates for design of multicolor LEDs⁶. Among rare earth ions, the dysprosium has attracted much attention due to its white light emission^{7,8}. Dy^{3+} ions emit several luminescence bands in blue, green, yellow and red ranges of the spectrum, which intensities depend on the host environment. As a host for Dy^{3+} doping, various matrices have been extensively studied such as phosphates^{9–11}, tungstate¹², vanadate¹³, molybdate¹⁴ niobate¹⁵, silicates^{16–18}, aluminate¹⁹, and borates^{20,21}. Orthovanadates have many exceptional characteristics including excellent thermal, mechanical, and optical properties; which play an important role in many optical devices, catalysts, and laser host materials^{22–24}. In particular, yttrium vanadate (YVO_4) is very significant oxide in materials science and technology, for example, its large single crystal has been extensively used as an excellent polarizer and laser host material, whereas its powder doped with several rare earth ions has been used as an attractive phosphor due to its high luminescence quantum yield^{25–27}. The previous works mainly focused on the Eu^{3+} -doped YVO_4 with different synthetic methods^{28–30}, because it is a commercial red-emitting phosphor used in color television, the high-pressure mercury lamp, and as a scintillator in medical image detectors^{31–34}. To the best of our knowledge, the systematic study of calcination

¹St. Petersburg State University, 7/9 Universitetskaya nab., 199034, St. Petersburg, Russia. ²Lappeenranta University of Technology LUT, Skinnarilankatu 34, 53850, Lappeenranta, Finland. ³Peter the Great St. Petersburg Polytechnic University, Polytechnicheskaya 29, 195251, St. Petersburg, Russia. ⁴Scientific and Technological Institute of Optical Material Science, VNTs S. I. Vavilov State Optical Institute, Babushkina 36-1, 192171, St. Petersburg, Russia. ⁵Volga State University of Technology, Lenin sq. 3, 424000, Yoshkar-Ola, Russia. Correspondence and requests for materials should be addressed to I.E.K. (email: ie.kolesnikov@gmail.com)

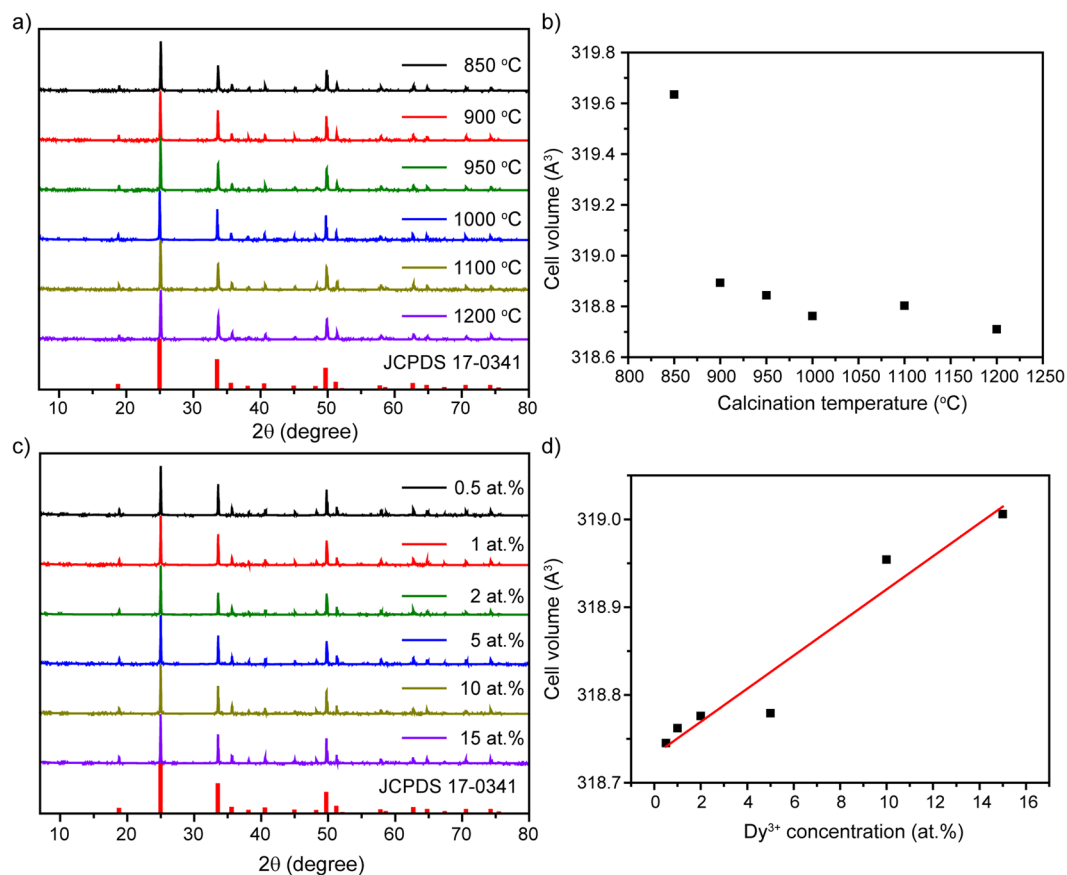


Figure 1. (a) XRD patterns of $\text{YVO}_4:\text{Dy}^{3+}$ 1 at.% temperature series and the standard card YVO_4 ; (b) unit cell volume as a function of calcination temperature; (c) XRD patterns of $\text{YVO}_4:\text{Dy}^{3+}$ 1000 °C concentration series and the standard card YVO_4 ; (d) unit cell volume as a function of Dy^{3+} -doping.

temperature and doping concentration effect on properties of $\text{YVO}_4:\text{Dy}^{3+}$ nanophosphors has not been reported so far.

Recently, great attention was attracted to developing of non-contact luminescence thermometers with sub-micrometric spatial resolution. One of the most promising thermal sensing techniques is based on luminescence intensity ratio between emission bands arising from two thermally coupled levels. These levels should be closely spaced (the energy gap generally ranges from 200 to 2000 cm^{-1}) and it is assumed to be in the thermodynamic quasi-equilibrium³⁵. The main advantage of the ratiometric approach for temperature sensing is independence on spectrum losses and fluctuations of the excitation intensity, which leads to a much higher accuracy^{36,37}. Emission bands of Dy^{3+} ions were originated from two thermally coupled levels ($^4\text{I}_{15/2}$ and $^4\text{F}_{9/2}$) with the energy difference around 1000 cm^{-1} . So, Dy^{3+} -doped nanoparticles is suitable for temperature sensing with high spatial resolution and good sensitivity, which can be used in organisms or in living cells^{36,38,39}.

This paper is focused on the detailed study of calcination temperature and doping concentration effect on the structure, steady-state and kinetics luminescence properties of $\text{YVO}_4:\text{Dy}^{3+}$ nanoparticles. Influence of excitation mechanisms on optimum doping concentration and quenching was explored. Synthesized samples were successfully used as ratiometric thermal sensors in wide temperature range of 298–673 K. The thermometric performances including thermal sensitivities, temperature uncertainty and repeatability were obtained.

Results and Discussion

Figure 1a shows XRD patterns of $\text{YVO}_4:\text{Dy}^{3+}$ 1 at.% samples prepared at different calcination temperatures. All diffraction peaks of powders can be indexed by the reference standard YVO_4 (tetragonal phase, space group 141/amd, JCPDS 17-0341). No other crystalline phase was detected. The cell parameters were calculated with UnitCell software. As it can be seen from Fig. 1b, unit cell volume decreases along with increase of calcination temperature. Such behavior can be elucidated by formation of better crystalline structure of nanoparticles with cell volume closer to the monocrystal⁴⁰.

Effect of Dy^{3+} doping concentration on YVO_4 nanocrystalline powders is presented in Fig. 1c. XRD patterns confirm the presence of pure tetragonal phase without any structural impurities. Dysprosium ions substitute yttrium ions in D_{2d} site symmetry. The single-crystal cell volume systematically increases with growth of dopant concentration due to the difference of ionic radii between yttrium ($r = 0.893 \text{ \AA}$) and dysprosium ions ($r = 1.03 \text{ \AA}$). Noteworthy, the unit cell volume has a linear relationship with the amount of Dy^{3+} , which is consistent with Vegard's law (Fig. 1d). This result demonstrates that the dysprosium ion has been efficiently and homogeneously

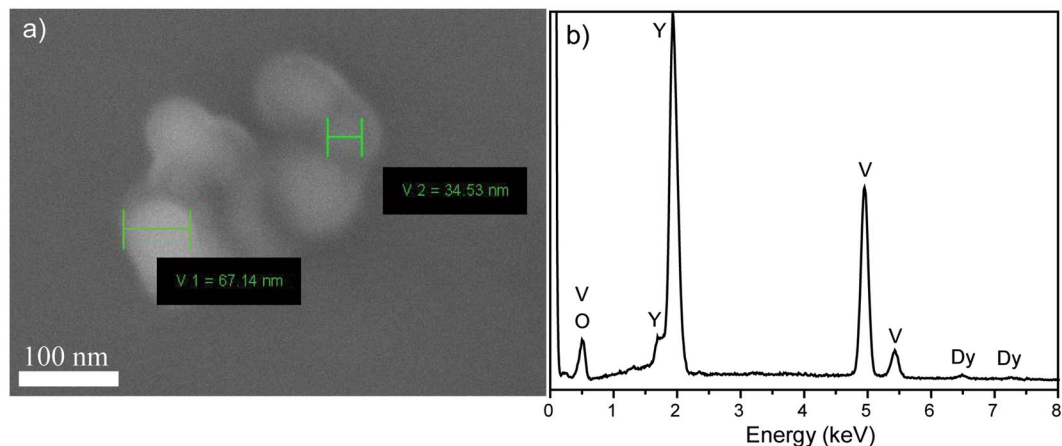


Figure 2. (a) SEM images of $\text{YVO}_4:\text{Dy}^{3+}$ 1 at.% 1000 °C nanopowder; (b) EDX analysis of $\text{YVO}_4:\text{Dy}^{3+}$ 1 at.% 1000 °C nanopowder.

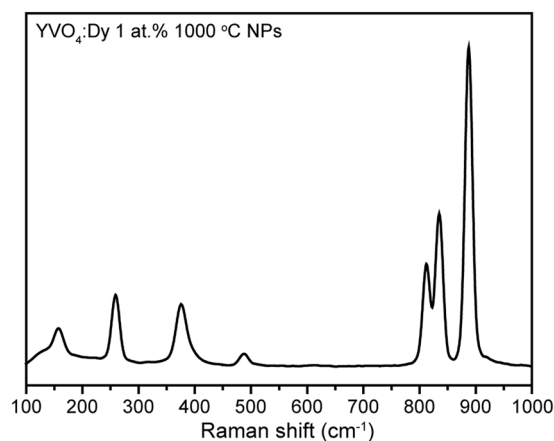


Figure 3. Raman spectrum of $\text{YVO}_4:\text{Dy}^{3+}$ 1 at.% 1000 °C nanopowder.

incorporated into the host matrix of YVO_4 due to the similar ionic radius and chemical reactivity of Dy^{3+} and Y^{3+} ⁴¹.

Figure 2a shows scanning electron microphotograph of the synthesized $\text{YVO}_4:\text{Dy}^{3+}$ 1 at.% 1000 °C nanopowder. As seen from the micrograph, the powder consists of weakly agglomerated nanoparticles with average size about 50 nm. Elemental analysis was studied using EDX technique. We observed signals from yttrium, vanadium, oxygen, and dysprosium (Fig. 2b).

Structural properties of Dy^{3+} -doped YVO_4 nanopowders were studied also using vibrational spectroscopy. Figure 3 presents Raman spectrum of $\text{YVO}_4:\text{Dy}^{3+}$ 1 at.% 1000 °C measured in spectroscopic range from 100 to 1000 cm^{-1} . As can be seen, this spectrum consists of several sharp Raman lines corresponding to the internal vibrations of VO_4^{3-} group and external vibrations of VO_4^{3-} tetrahedra and Y^{3+} ions in YVO_4 unit cell⁴². The external vibration at 157 cm^{-1} ($\text{B}_{1g}(1)$) can be attributed to the O–Y–O bending mode. The internal vibrations, which can be ascribed to the O–V–O bending and VO_4 stretching modes, are located at higher frequencies: 259 (B_{2g}), 376 ($\text{A}_{1g}(1)$), 488 ($\text{B}_{1g}(3)$), 812 ($\text{B}_{1g}(4)$), 835 ($\text{E}_g(5)$) and 888 cm^{-1} ($\text{A}_{1g}(2)$)⁴³. The observed spectrum is dominated by the totally symmetrical vibration of VO_4^{3-} tetrahedron³². Narrow width of Raman lines indicates good crystallinity and homogeneity of synthesized powder.

Further investigations were devoted to the influence of synthesis conditions (calcination temperature and doping concentration) on luminescence properties. Figure 4a shows excitation spectra within spectral range of 260–560 nm ($\lambda_{\text{em}} = 573$ nm) for nanocrystalline powders $\text{YVO}_4:\text{Dy}^{3+}$ 1 at.% calcinated at different temperatures. The obtained spectra consist of broad and intense band in the UV region and several narrow lines in visible region. The broad band can be assigned to the charge transfer from the oxygen ligands to the central vanadium atom inside the VO_4^{3-} groups⁴⁴. From the viewpoint of molecular orbital theory, it corresponds to transitions from the $^1\text{A}_2$ ($^1\text{T}_1$) ground state to $^1\text{A}_1$ (^1E) and ^1E ($^1\text{T}_2$) excited states of the VO_4^{3-} ion⁴⁵. Low peaks in visible region at longer wavelength are assigned to the intra-configurational 4f–4f transitions in dysprosium ions. The observed bands are attributed to the following transitions: $^6\text{H}_{15/2} - ^4\text{P}_{7/2}$ (352 nm), $^6\text{H}_{15/2} - ^4\text{P}_{5/2}$ (365 nm), $^6\text{H}_{15/2} - ^4\text{I}_{13/2}$ (387 and 390 nm), $^6\text{H}_{15/2} - ^4\text{G}_{11/2}$ (427 nm), $^6\text{H}_{15/2} - ^4\text{I}_{15/2}$ (449 and 453 nm) and $^6\text{H}_{15/2} - ^4\text{F}_{9/2}$ (473 nm).

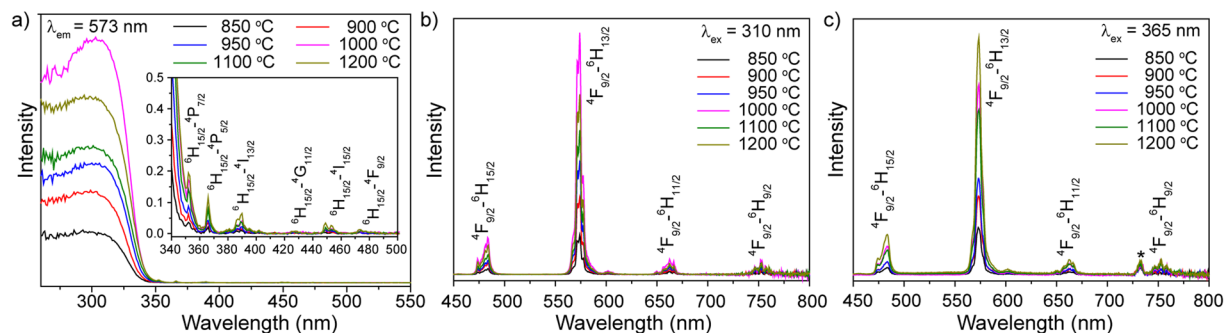


Figure 4. (a) Excitation spectra of $\text{YVO}_4:\text{Dy}^{3+}$ 1 at.% nanopowders calcinated at different temperatures ($\lambda_{\text{em}} = 573$ nm). Emission spectra of $\text{YVO}_4:\text{Dy}^{3+}$ 1 at.% nanopowders calcinated at different temperatures upon (b) $\lambda_{\text{ex}} = 310$ nm and (c) $\lambda_{\text{ex}} = 365$ nm excitation. The asterisk indicates the second order of excitation wavelength.

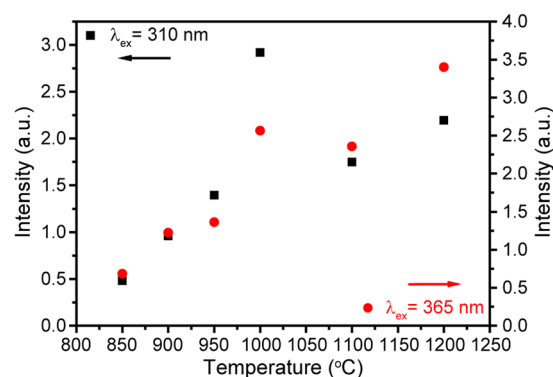


Figure 5. Dependence of ${}^4\text{F}_{9/2}\text{-}{}^6\text{H}_{13/2}$ integrated intensity of $\text{YVO}_4:\text{Dy}^{3+}$ 1 at.% nanopowders on calcination temperature.

Emission spectra of nanocrystalline powders $\text{YVO}_4:\text{Dy}^{3+}$ 1 at.% calcinated at different temperatures are shown in Fig. 4b,c. The measurements were conducted in the spectral range of 450–800 nm upon $\lambda_{\text{ex}} = 310$ nm and 365 nm radiation, which presents various excitation mechanisms. The emission spectra are dominated by green-yellow band (573 nm) corresponding to the hypersensitive ${}^4\text{F}_{9/2}\text{-}{}^6\text{H}_{13/2}$ transition. Other observed lines are attributed to the ${}^4\text{I}_{15/2}\text{-}{}^6\text{H}_{15/2}$ (455 nm), ${}^4\text{F}_{9/2}\text{-}{}^6\text{H}_{15/2}$ (484 nm), ${}^4\text{F}_{9/2}\text{-}{}^6\text{H}_{11/2}$ (662 nm), ${}^4\text{F}_{9/2}\text{-}{}^6\text{H}_{9/2}$ (752 nm) transitions. ${}^4\text{F}_{9/2}\text{-}{}^6\text{H}_{13/2}$ is the forced electric dipole transition, which is hypersensitive and its intensity can vary by orders of magnitude depending on the local site symmetry, whereas ${}^4\text{F}_{9/2}\text{-}{}^6\text{H}_{15/2}$ transition intensity is insignificantly affected by the environment^{46,47}.

Integrated intensity of the most prominent ${}^4\text{F}_{9/2}\text{-}{}^6\text{H}_{13/2}$ transition upon $\lambda_{\text{ex}} = 310$ and 365 nm radiation versus calcination temperature is shown in Fig. 5. As one can see, increase of calcination temperature leads to the growth of emission intensity, which coincides with usual behavior of rare earth-doped nanomaterials^{48–50}. The observed growth is explained by an improvement of the sample crystallinity and a decrease of the number of OH^- groups on the surface of nanoparticles^{51,52}. In addition, it is well known that a growth of the calcination temperature leads to an increase of nanoparticles size, which in turn also results in luminescence intensity enhancement due to reduction of doping ions fraction on the surface⁵³.

To get more information about photoluminescence characteristics of prepared nanophosphors, fluorescence kinetics measurements were carried out. The photoluminescence decays of $\text{YVO}_4:\text{Dy}^{3+}$ temperature series were monitored at ${}^4\text{F}_{9/2}\text{-}{}^6\text{H}_{13/2}$ transition upon 310 nm excitation (Fig. 6a). All experimental curves were fitted by single exponential function:

$$I = I_0 \cdot e^{-\frac{t}{\tau_f}} \quad (1)$$

where τ_f is the observed lifetime of ${}^4\text{F}_{9/2}$ level. Figure 6b shows measured lifetimes dependence on calcination temperature. It should be noted that the increase of calcination temperature insignificantly affects the ${}^4\text{F}_{9/2}$ lifetime.

Next we discuss the effect of doping concentration on the luminescence properties of nanocrystalline powders $\text{YVO}_4:\text{Dy}^{3+}$. All samples of concentration series (1–15 at.%) were synthesized with calcination temperature of 1000 °C. Excitation spectra of nanocrystalline powders $\text{YVO}_4:\text{Dy}^{3+}$ 1000 °C with different doping concentrations are shown in Fig. 7a. These spectra consist of intense band attributed to the absorption of VO_4^{3-} groups and weak Dy^{3+} 4f–4f transitions as it was described for temperature series. The spectral line positions of concentration

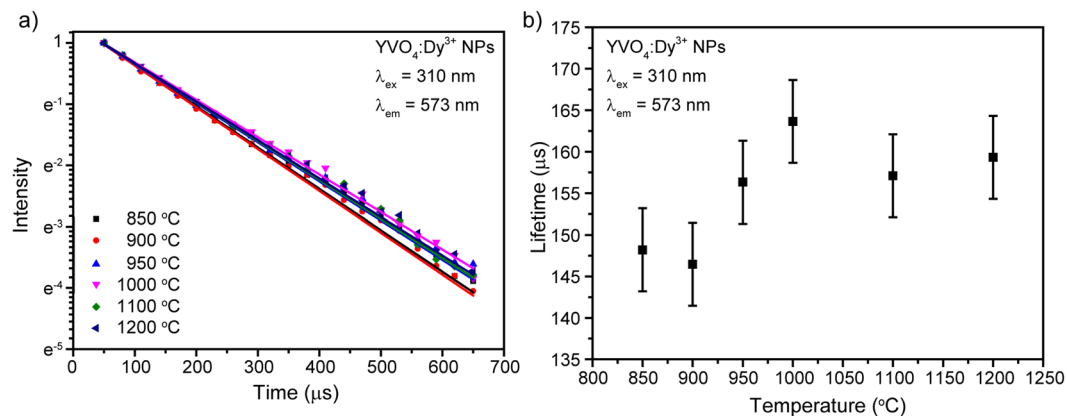


Figure 6. (a) Decay curves of YVO₄:Dy³⁺ 1 at.% temperature series; (b) ⁴F_{9/2} lifetime as a function of calcination temperature.

series coincide with the temperature series. Emission spectra of nanocrystalline powders YVO₄:Dy³⁺ 1000 °C with different doping concentrations upon 310 nm and 365 nm radiation are presented in Fig. 7b,c. The most intensive line in the measured spectra is attributed to the ⁴F_{9/2}-⁶H_{13/2} transition.

Figure 8 presents the integrated luminescence intensity of the most intensive transition ⁴F_{9/2}-⁶H_{13/2} as a function of doping concentration upon excitation wavelengths 310 and 365 nm. It is well-known that the optimum of Dy³⁺ concentration is determined by two competitive effects: on the one hand, an increase of the doping concentration means an increase of luminescence centers number and thus radiative recombination. On the other hand, there is also an increase of the probability of energy transfer between dysprosium ions, which enhances the efficiency of the nonradiative processes⁵⁴. As can be seen, first emission intensity goes up with increasing doping concentration but further growth of Dy³⁺ ions number leads to intensity reduction. This indicates the concentration quenching effects for the luminescence of Dy³⁺ in YVO₄ host. Noteworthy, the optimum doping concentration was found to be different for various excitation mechanisms. The optimum Dy³⁺ concentration for host excitation (310 nm) was determined to be 1 at.%, whereas for the direct Dy³⁺ ions excitation (365 nm) optimum concentration was 2 at.%. Similar difference in optimum concentration depending on excitation mechanism was previously observed for Eu³⁺ and Nd³⁺-doped YVO₄ nanopowders^{32,55}.

To obtain information about Dy³⁺ concentration effect on the crystal structure and crystal field, ratio between ⁴F_{9/2}-⁶H_{13/2} and ⁴F_{9/2}-⁶H_{15/2} intensities (*R*) was calculated. This parameter is similar to the well-known asymmetry ratio for Eu³⁺ ions^{56,57}. *R* value give information about the local surrounding and environmental changes near the Dy³⁺ ions. The higher the calculated parameter is, the more apart from a centrosymmetric geometry luminescent center is located. It is well-known that if Dy³⁺ is located at low symmetry without the inversion symmetry, the yellow emission is the most intense of all the transitions, as is the case with our synthesized nanocrystalline phosphors⁵⁸. Figure 9 shows the dependence of *R* value, calculated from emission spectra obtained upon 365 nm excitation, on Dy³⁺ doping concentration for YVO₄ host. As can be seen, the calculated ratio demonstrates non-monotonical behavior, but main trend is decreasing of *R* value along with increasing of doping concentration. So, we can conclude that introduction of additional Dy³⁺ ions in YVO₄ host results in growth of local symmetry.

Luminescence decays of YVO₄:Dy³⁺ concentration series monitored at ⁴F_{9/2}-⁶H_{13/2} transition upon 310 nm excitation are presented in Fig. 10a. Experimental data of synthesized nanocrystalline powders doped with 0.5 and 1 at.% were approximated by mono-exponential function. Higher doped samples demonstrate non mono-exponential decay, therefore, to provide correct fitting we used biexponential model. The average lifetime was obtained according following formula⁵⁹:

$$\tau_{av} = \frac{A_1\tau_1^2 + A_2\tau_2^2}{A_1\tau_1 + A_2\tau_2} \quad (2)$$

where *A*₁ and *A*₂ are pre-exponential factors; τ_1 and τ_2 are lifetimes. The fitting model was changed due to growth of Dy³⁺ doping ions located on the nanopartilces surface⁶⁰. The non mono-exponential behavior is originated from the different decay rates of the Dy³⁺ ions situated at the surface and in the volume of the nanoparticles⁶¹⁻⁶³. Figure 10b shows dependence of the obtained lifetimes on Dy³⁺ doping concentration. One can see that the lifetime gradually declines from 163 μs to 69 μs along with increase of Dy³⁺ ions number.

As it was previously observed, growth of the amount of Dy³⁺ ions in YVO₄ host leads to the concentration quenching. According to Blasse *et al.*, the energy transfer mechanism is defined by the critical energy transfer distance (*R_c*) if the doping ions occupy single crystallographic position. The critical energy transfer distance was calculated by the following equation⁶⁴:

$$R_c \approx 2 \left[\frac{3V}{4\pi x_c N} \right]^{\frac{1}{3}} \quad (3)$$

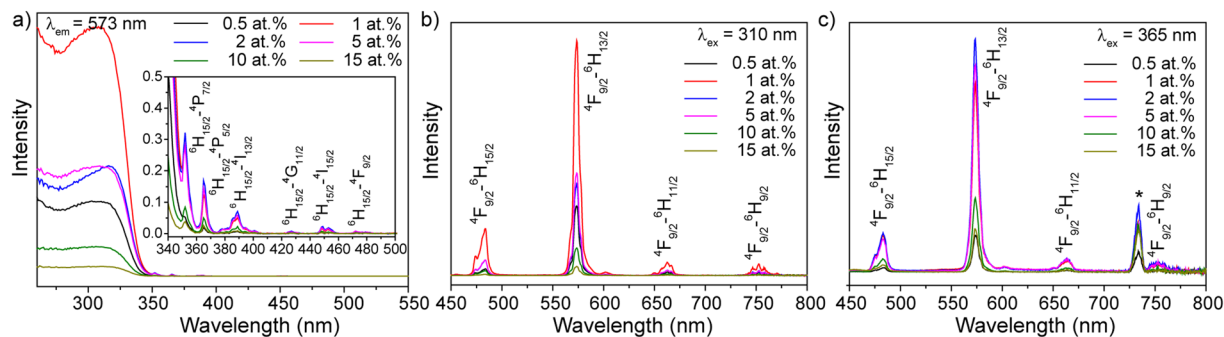


Figure 7. (a) Excitation spectra of $\text{YVO}_4:\text{Dy}^{3+}$ 1000 °C nanopowders with different doping concentrations ($\lambda_{\text{em}} = 573$ nm). Emission spectra of $\text{YVO}_4:\text{Dy}^{3+}$ 1000 °C nanopowders with different doping concentrations upon (b) $\lambda_{\text{ex}} = 310$ nm and (c) $\lambda_{\text{ex}} = 365$ nm excitation. The asterisk indicates the second order of excitation wavelength.

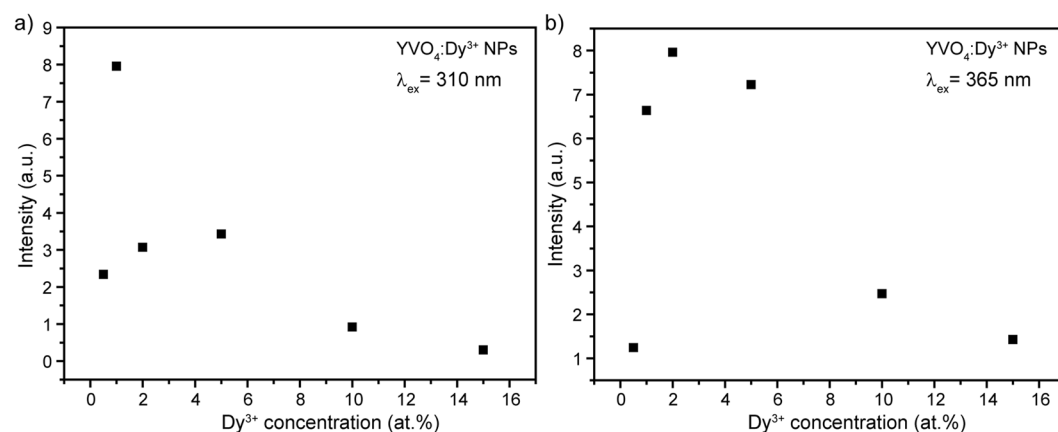


Figure 8. Dependence of ${}^4\text{F}_{9/2}\text{-}{}^6\text{H}_{13/2}$ integrated intensity of $\text{YVO}_4:\text{Dy}^{3+}$ nanopowders on doping concentration upon (a) 310 nm and (b) 365 nm excitation.

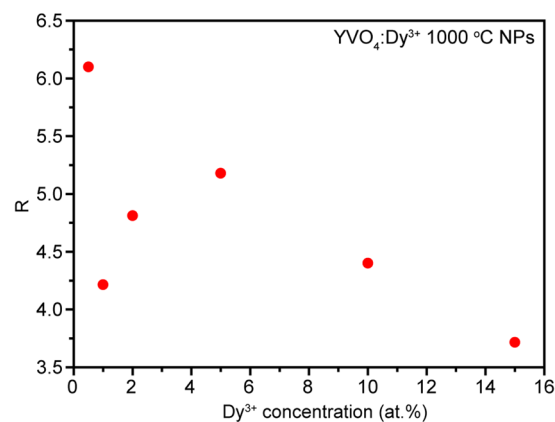


Figure 9. ${}^4\text{F}_{9/2}\text{-}{}^6\text{H}_{13/2} / {}^4\text{F}_{9/2}\text{-}{}^6\text{H}_{15/2}$ intensity ratio of $\text{YVO}_4:\text{Dy}^{3+}$ samples as a function of doping concentration.

where x_c is the critical doping content ($x_c = 0.01$ or 0.02), N is the number of cation sites in the unit cell ($N = 4$ for YVO_4), and V is the volume of the unit cell ($V \approx 318.78 \text{ \AA}^3$). Using aforementioned parameters, R_c was found to be 24.8 and 19.6 \AA for host and direct excitations, respectively. Upon both excitation wavelengths calculated value of R_c is bigger than 5 \AA , so exchange interaction cannot control energy transfer between Dy^{3+} ions in YVO_4 host⁶⁵. Therefore, we can conclude that the concentration quenching is caused by the multipolar interaction mechanism^{66,67}. Multipolar interaction includes dipole-dipole (d-d), dipole-quadrupole (d-q), and

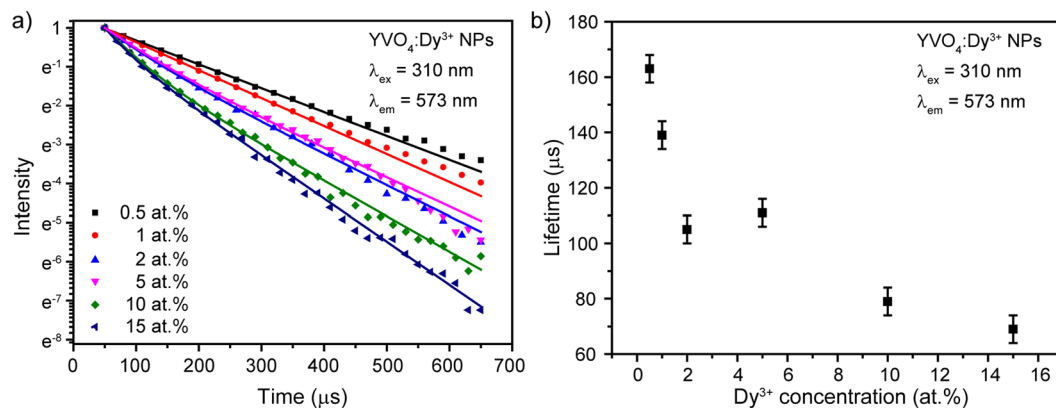


Figure 10. (a) Decay curves of YVO₄:Dy³⁺ concentration series; (b) ⁴F_{9/2} level lifetime as a function of doping concentration.

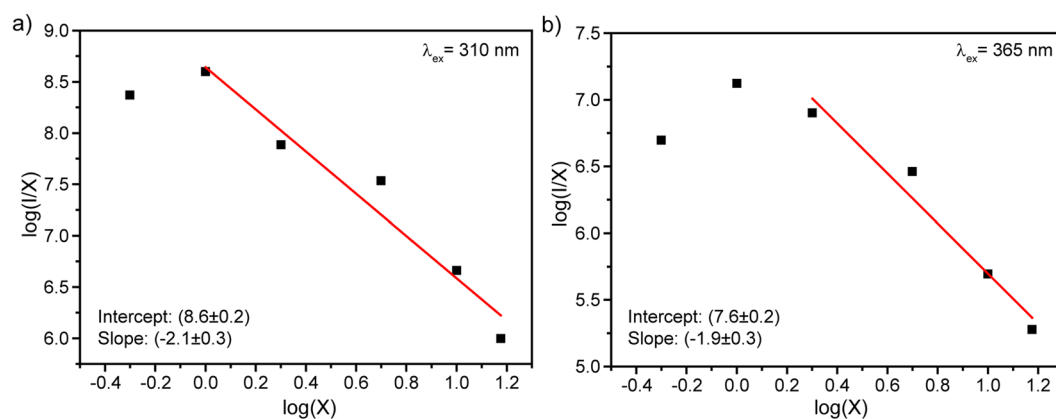


Figure 11. Logarithmic plot of YVO₄:Dy³⁺ nanophosphors emission intensity vs doping concentration upon (a) 310 nm and (b) 365 nm excitation. Lines are a linear fit.

quadrupole–quadrupole (q–q) interaction. An interaction type can be determined using formula proposed by Van Uitert⁶⁸. Further, Ozawa and Jaffe modified it as follows⁶⁹:

$$\frac{I}{x} = k \left[1 + \beta(x)^{\frac{\theta}{3}} \right]^{-1} \quad (4)$$

where I is the integral intensity, x is the activator concentration, k and β are constant for the same excitation conditions for a given host crystal. According to the above equation $\theta = 3$ for the energy transfer among the nearest neighbor ions, while $\theta = 6, 8$ and 10 for d–d, d–q and q–q interactions, respectively^{70,71}.

The critical concentration of Dy³⁺ ions was determined as 1 and 2% for 310 and 365 nm excitation, respectively. The dependence of the emission intensity of YVO₄:Dy³⁺ nanopowders on the doping concentration was investigated. The multipolar character (θ) can be obtained by plotting $\log(I/x)$ vs $\log(x)$ as presented in Fig. 11. The slope $\theta/3$ from approximation was determined to be -2.06 and -1.89 for 310 and 365 nm excitation, giving calculated value of θ is close to 6 in both cases. Therefore, concentration quenching in YVO₄:Dy³⁺ nanocrystalline powders occurred due to dipole–dipole interaction regardless of the excitation mechanism.

In order to study the emission color dependence of the synthesized nanophosphors on calcination temperature and doping concentration, the Commission Internationale de L'Éclairage (CIE) chromaticity coordinates were calculated and the results are presented in Fig. S1 and Table 1. The chromaticity coordinates were obtained using emission spectra measured upon 310 nm excitation. As can be seen, both calcination temperature and doping concentration do not strongly influence on the emission color of Dy³⁺-doped YVO₄ phosphor. Moreover, it should be noted that the observed small change of CIE coordinates has nonmonotonic behavior along with growth of calcination temperature or Dy³⁺ concentration.

During last decade a lot of attention is attracted to the search of convenient non-contact luminescence thermometer^{72–74}. Due to the unique properties of rare earth ions, plenty organic and inorganic materials doped with lanthanides has been suggested for luminescence thermometry^{75–77}. Here, we studied possibility to define local temperature using Dy³⁺-doped YVO₄ nanophosphors.

Sample	CIE chromaticity coordinates	
	x	y
Temperature series		
850 °C	0.440	0.486
900 °C	0.439	0.486
950 °C	0.444	0.490
1000 °C	0.438	0.485
1100 °C	0.441	0.487
1200 °C	0.435	0.483
Concentration series		
0.5 at.%	0.449	0.498
1 at.%	0.425	0.474
2 at.%	0.433	0.480
5 at.%	0.436	0.485
10 at.%	0.431	0.479
15 at.%	0.444	0.490

Table 1. CIE coordinates of $\text{YVO}_4:\text{Dy}^{3+}$ temperature and concentration series.

Figure 12 shows normalized emission spectra of $\text{YVO}_4:\text{Dy}^{3+}$ 1 at.% and 2 at.% nanopowders measured at different temperatures (298, 423 and 673 K). The observed emission lines are originated from electron transitions from $^4\text{I}_{15/2}$ and $^4\text{F}_{9/2}$ excited states with energy separation of about 1000 cm^{-1} (Fig. 12c). According to definition, $^4\text{I}_{15/2}$ and $^4\text{F}_{9/2}$ are thermally coupled levels, therefore ratiometric approach for transitions from these excited states can be utilized to determine local temperature. Luminescence intensity ratio (LIR) between $^4\text{I}_{15/2}-^6\text{H}_{15/2}$ and $^4\text{F}_{9/2}-^6\text{H}_{15/2}$ transitions ($R_{455/480}$), as well as ratio between $^4\text{I}_{15/2}-^6\text{H}_{15/2}$ and $^4\text{F}_{9/2}-^6\text{H}_{13/2}$ transitions ($R_{455/575}$) were used for thermal sensing. It should be noted that calculation of luminescence ratios was based on the integrated intensities of transitions, because such approach gives better accuracy comparing with peak intensities⁷⁸.

The variations of the LIR values of $\text{YVO}_4:\text{Dy}^{3+}$ 1 at.% and $\text{YVO}_4:\text{Dy}^{3+}$ 2 at.% nanocrystalline powders as a function of the temperature are presented in Fig. 13. Temperature induced change of LIR is caused by electron re-distribution at the energy levels according to the Boltzmann formula:

$$R = A \cdot \exp\left(-\frac{\Delta E}{kT}\right) \quad (5)$$

where A is a temperature-independent constant, ΔE is the energy gap between thermally coupled energy levels, k is the Boltzmann's constant and T is the absolute temperature. As can be seen, the experimental data were successfully fitted with eq. (5) and the obtained parameters were presented in the graphs.

To estimate the performance of the thermometer, absolute (S_a) and relative (S_r) thermal sensitivities are usually used. The absolute thermal sensitivity shows the absolute LIR change with temperature variation and is defined as follows:

$$S_a = \frac{dR}{dT} = R \frac{\Delta E}{kT^2} \quad (6)$$

It is obviously from Eq. (6) that S_a depends on absolute LIR value, which can be significantly changed by manipulating LIR calculation procedure (for instance, change of integration limit for calculation of integral intensity of emission transition). Therefore, absolute thermal sensitivity cannot be used for the fair comparison among different systems⁷⁹. To compare thermometers irrespective to their nature and sensing parameter, the relative thermal sensitivity is introduced. S_r shows normalized change of LIR with temperature variation and is defined as follows:

$$S_r = \frac{1}{R} \frac{dR}{dT} = \frac{\Delta E}{kT^2} \quad (7)$$

The variation of the S_a and S_r value with temperature from 298 to 673 K for both studied LIRs is presented in the Fig. 14. The observed temperature dependences of S_a and S_r demonstrate opposite behavior: temperature increase leads to the gradual growth of S_a and monotonic decline of S_r . Temperature dependence in both studied LIRs is originated from the same excited levels: $^4\text{I}_{15/2}$ and $^4\text{F}_{9/2}$. So, it is unsurprising that the maximal relative thermal sensitivity ($T = 298\text{ K}$) for $R_{455/480}$ and $R_{455/575}$ ratios is similar: $1.8\% \text{ K}^{-1}$ ($\text{YVO}_4:\text{Dy}^{3+}$ 1 at.%) and $1.5\% \text{ K}^{-1}$ ($\text{YVO}_4:\text{Dy}^{3+}$ 2 at.%). However, the absolute thermal sensitivities differ significantly: $0.039 \text{ K}^{-1}@673\text{ K}$ ($R_{455/480}$) and $0.0013 \text{ K}^{-1}@673\text{ K}$ ($R_{455/575}$) in case of $\text{YVO}_4:\text{Dy}^{3+}$ 1 at.%. Noteworthy that increase of Dy^{3+} doping concentration results in worsening of thermal sensitivity.

In comparison with Er^{3+} , Tm^{3+} or Nd^{3+} ions, dysprosium ions are relatively rare utilizing for temperature sensing. Among other Dy^{3+} single doped materials, the obtained S_r values are comparable to the values reported in the literature: $1.7\% \text{ K}^{-1}$ for $\text{BaYF}_5:\text{Dy}^{3+}$ NPs⁸⁰, $1.6\% \text{ K}^{-1}$ for $\text{Gd}_2\text{Ti}_2\text{O}_7:\text{Dy}^{3+}$ NPs⁸¹, $1.7\% \text{ K}^{-1}$ for $\text{YAG}:\text{Dy}^{3+}$ microcrystals⁸², $1.7\% \text{ K}^{-1}$ and $1.3\% \text{ K}^{-1}$ for $\text{Dy}:\text{Y}(\text{acac})_3$ and $\text{Dy}:\text{Y}(\text{acac})_3(\text{phen})$ molecular crystals, respectively⁸³.

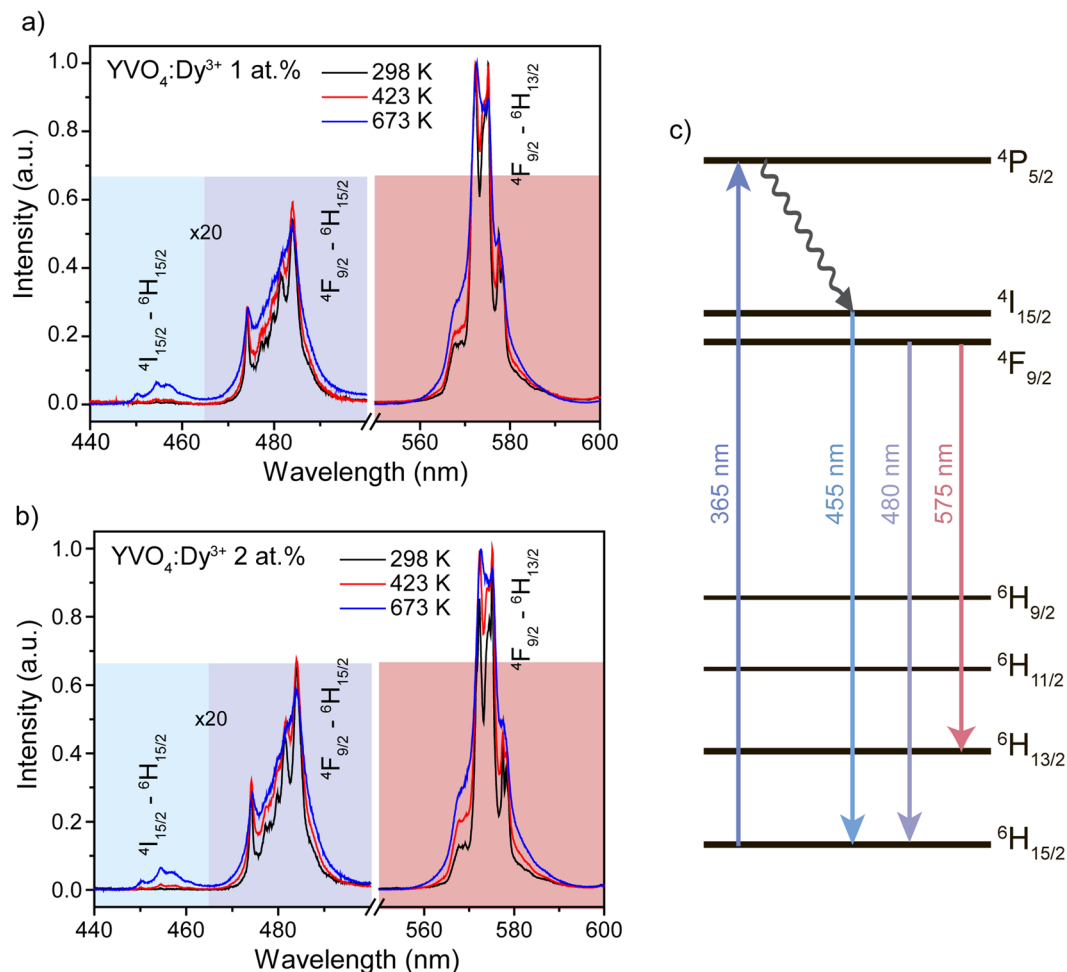


Figure 12. Normalized emission spectra of (a) YVO₄:Dy³⁺ 1 at.% and (b) YVO₄:Dy³⁺ 2 at.% nanopowders at different temperatures. The colored areas are used for the integral intensity ratio calculations. (c) Energy levels scheme of YVO₄:Dy³⁺ nanophosphors.

The minimum temperature uncertainty (ΔT) provides information about accuracy of thermal sensing which can be derived using this material. There are several experimental techniques to obtain minimum temperature uncertainty, which were discussed and compared in our previous work⁷⁸. Here, ΔT was estimated from consecutive emission spectra measured at fixed heating stage temperature (Figs S2 and S3). Due to the rather wide temperature sensing region, temperature uncertainty was obtained for 323 and 473 K. The obtained value of ΔT is lying in the range of 2–7 K depending on the measured temperature, used luminescence intensity ratio and doping concentration.

Third important factor for the assessment of the precision of a thermometric system is repeatability. We tested repeatability of YVO₄:Dy³⁺ thermometers over cyclic heating-cooling measurements (Fig. 15). During the experiment, we increased and decreased the temperature within the thermal range of 323–473 K. Black squares indicate the actual temperature of heater, whereas red circles and blue triangles present temperature obtained with $R_{455/480}$ and $R_{455/575}$ luminescence intensity ratio, respectively. Taking into account temperature uncertainty, we can conclude good repeatability of considered YVO₄:Dy³⁺ nanopowders: temperatures obtained using optical thermometry are repeated from cycle to cycle and they are in good agreement with the actual heater temperature.

Summary

Series of nanocrystalline Dy³⁺-doped YVO₄ samples with different calcination temperature and doping concentration were prepared by modified Pechini method. XRD study defines that YVO₄:Dy³⁺ nanoparticles had tetragonal phase without any impurities. Synthesized samples consisted of quite small nanoparticles with size about 50 nm. EDX technique revealed signals from yttrium, vanadium, oxygen, and dysprosium. Narrow width of Raman lines confirmed good homogeneity and crystallinity of synthesized nanoparticles. Excitation spectrum of Dy³⁺-doped YVO₄ nanophosphors consisted of broad band and several narrow lines assigned to the pump through matrix host and direct pump of Dy³⁺ ion, respectively. Emission spectrum consisted of the characteristic narrow lines attributed to the intra-configurational 4f-4f transitions. The most intensive luminescence band corresponded to the hypersensitive $4F_{9/2} - {}^6H_{13/2}$ transition. Calcination temperature increase led to the growth of emission intensity due to the improvement of the crystallinity and decrease of the quenchers number. Study

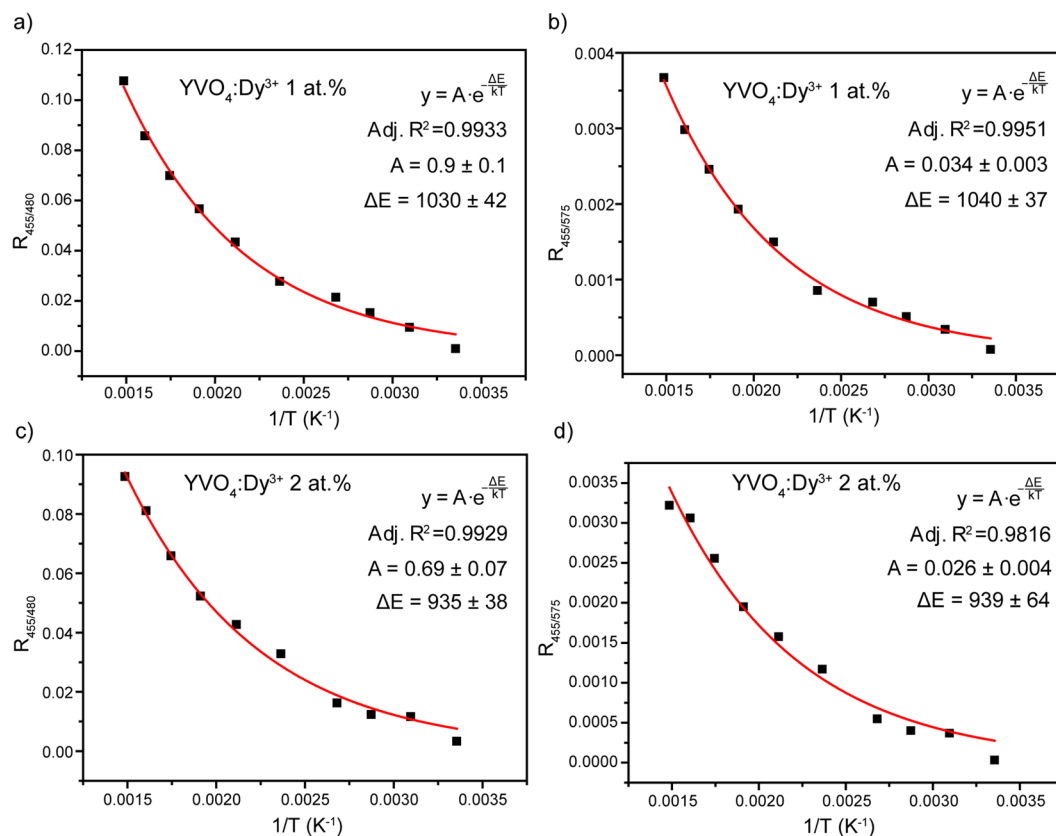
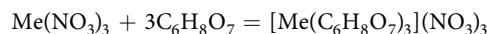


Figure 13. Luminescence intensity ratio ($R_{455/480}$) of (a) $\text{YVO}_4:\text{Dy}^{3+}$ 1 at.% and (c) $\text{YVO}_4:\text{Dy}^{3+}$ 2 at.% nanopowders as a function of temperature. Luminescence intensity ratio ($R_{455/575}$) of (b) $\text{YVO}_4:\text{Dy}^{3+}$ 1 at.% and (d) $\text{YVO}_4:\text{Dy}^{3+}$ 2 at.% nanopowders as a function of temperature. Red lines correspond to the best fitting with Eq. (5).

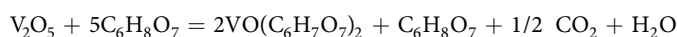
of $\text{YVO}_4:\text{Dy}^{3+}$ concentration series demonstrated usual concentration quenching effect. The optimal Dy^{3+} doping concentrations of 1 and 2 at.% were determined for different excitation mechanisms ($\lambda_{\text{ex}} = 310$ and 365 nm, respectively). Concentration quenching in $\text{YVO}_4:\text{Dy}^{3+}$ nanocrystalline powders occurred due to dipole–dipole interaction regardless of the excitation mechanism. The calcination temperature variation did not affect $^4\text{F}_{9/2}$ lifetime, whereas increase of doping concentration resulted in its gradual decline. CIE coordinates of $\text{YVO}_4:\text{Dy}^{3+}$ nanoparticles did not depend on either calcination temperature or doping concentration. $\text{YVO}_4:\text{Dy}^{3+}$ 1 at.% and $\text{YVO}_4:\text{Dy}^{3+}$ 2 at.% nanocrystalline powders were tested as ratiometric luminescence thermometers. Temperature sensing based on $R_{455/480}$ and $R_{455/575}$ luminescence intensity ratios was demonstrated within wide thermal range of 298–673 K. The maximum relative thermal sensitivity was 1.8% K^{-1} @ 298 K, whereas the minimum temperature uncertainty was found to be 2 K. Thermal cycling experiments showed good repeatability of studied thermometer.

Methods

$\text{YVO}_4:\text{Dy}^{3+}$ samples were prepared by modified Pechini method^{32,55}. The doping concentration of Dy^{3+} was 0.5, 1, 2, 5, 10, 15 at.% to Y^{3+} in YVO_4 host. The starting materials were yttrium oxide (Y_2O_3), dysprosium oxide (Dy_2O_3), vanadium oxide (V_2O_5), concentrated nitric acid (HNO_3), citric acid ($\text{C}_6\text{H}_8\text{O}_7$) and ethylene glycol ($\text{C}_2\text{H}_6\text{O}_2$). Y_2O_3 and Dy_2O_3 were dissolved in concentrated HNO_3 with heated to form nitrates solution. Then aqueous solution of citric acid was added to yttrium-dysprosium nitrates mixture (with volume ratio 1:1). The chemical reaction is as follows:



Then V_2O_5 was dissolved in citric acid to form $\text{VO}(\text{C}_6\text{H}_7\text{O}_7)_2$ according to the following reaction:



After that previous metals citrate complex ($[\text{Me}(\text{C}_6\text{H}_8\text{O}_7)_3](\text{NO}_3)_3$) was added with stirring and heated. The green solution was formed. Then ethylene glycol was added to the above mixture (volume ratio with of ethylene glycol and citric acid solution was 1:4 respectively). The formation of citrate transparent gel was observed. The obtained polymer gel was transferred to a crucible and then was placed in a furnace maintained at a temperature of 500 °C/1 h to burn off the organic components. The brown powder was formed. It was grinded in mortar with

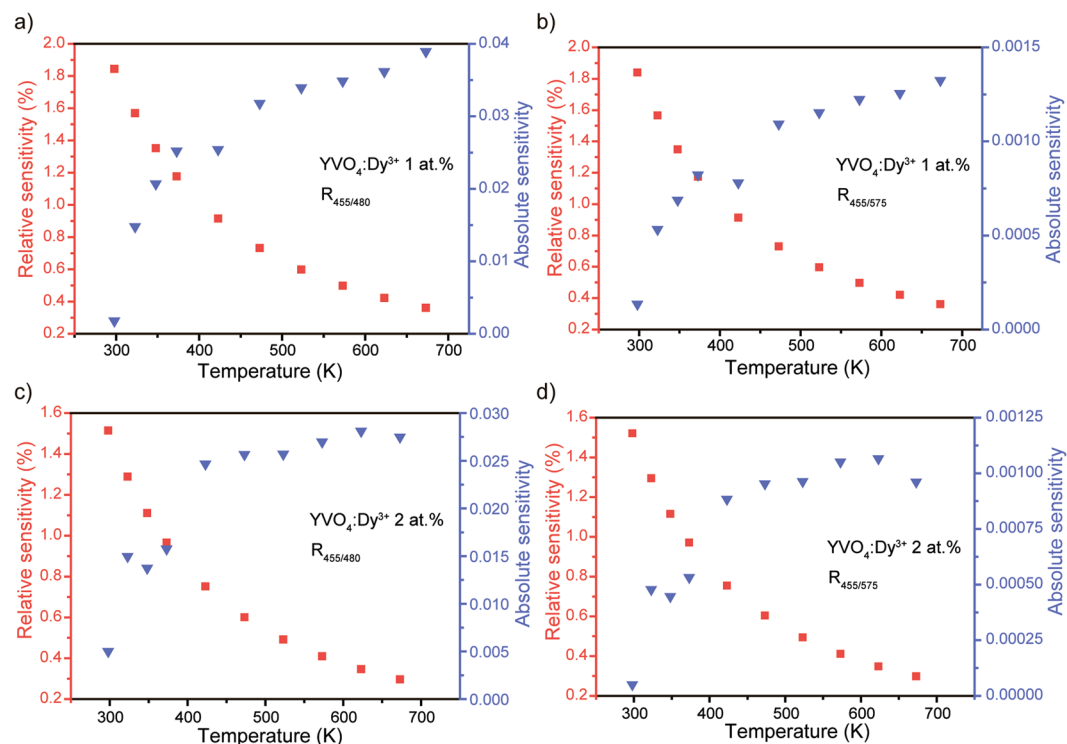


Figure 14. Variation of absolute (S_a) and relative (S_r) thermal sensitivity dependence on temperature for (a,b) YVO₄:Dy³⁺ 1 at.% and (c,d) YVO₄:Dy³⁺ 2 at.%.

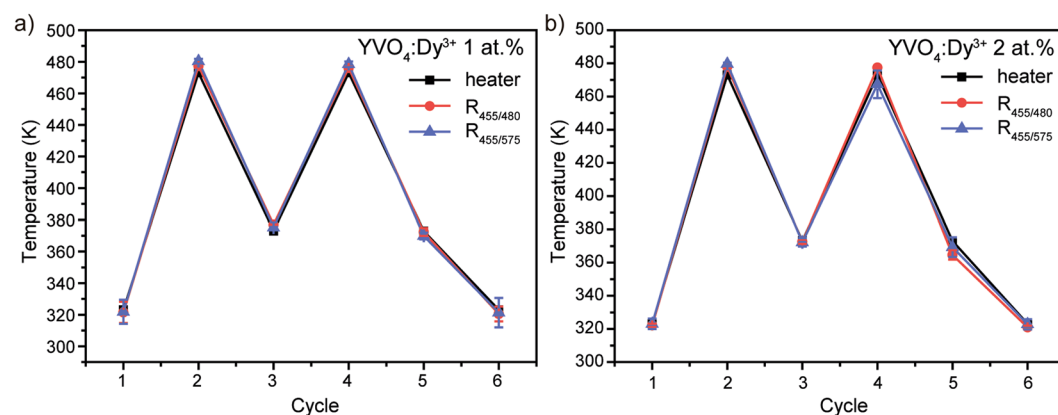


Figure 15. Calculated and measured temperature in heating-cooling cycles for (a) YVO₄:Dy³⁺ 1 at.% and (b) YVO₄:Dy³⁺ 2 at.%.

adding the potassium chloride in weight ratio 1:1. Then powder mixture kept in a muffle furnace maintained at predefined temperature/1.5 h. We used 850, 900, 950, 1000, 1100 and 1200 °C as the second calcination temperature. After the second thermal treatment white powder was removed from the furnace, centrifuged, washed three times with distilled water to remove potassium chloride and, finally, dried. Thus, YVO₄:Dy³⁺ nanocrystalline powders were synthesized.

X-ray diffraction patterns were registered with the powder diffractometer UltimaIV (Rigaku) in Bragg-Brentano geometry with CuK α 1 radiation ($\lambda = 1.54059 \text{ \AA}$) in the 2θ range from 7° to 80°. Phase identification was carried out using a powder diffraction database PowderDiffractionFile (PDF-2, 2011). The unit cell parameters were estimated using UnitCell software. Electron micrograph images and elemental analysis were obtained using Zeiss Merlin electron microscope with Oxford Instruments INCAx-act accessory. Raman spectrum was measured on Bruker SENTERRA Raman Microscope with semiconductor laser 488 nm as an excitation source. Steady-state and kinetics photoluminescence properties were studied with modular fluorescence spectrometer Fluorolog-3 (HORIBA Jobin Yvon). All thermal measurements were performed by using T64000 Raman Spectrometer. The Dy³⁺-doped YVO₄ NPs were optically excited with a 374 nm diode laser Coherent CUBE. The laser beam was

focused into the sample by using a 4x long working distance microscope objective (NA 0.1). The fluorescence was collected by using the same microscope objective and was spectrally analyzed by single spectrometer and Peltier cooled Synapse CCD detector. The temperature was controlled with a heating stage controlled with heating stage Linkam TS1000 with 0.1 °C temperature stability and 0.1 °C set point resolution.

References

- Wang, G., Peng, Q. & Li, Y. Lanthanide-doped nanocrystals: synthesis, optical-magnetic properties, and applications. *Acc. Chem. Res.* **44**, 322–332 (2011).
- Zhuang, J. *et al.* Controlled hydrothermal growth and up-conversion emission of NaLnF₄ (Ln = Y, Dy–Yb). *Inorg. Chem.* **46**, 5404–5410 (2007).
- Li, L. *et al.* Luminescence of Ce³⁺ in different lattice sites of La₂CaB₁₀O₁₉. *J. Phys. Chem. C* **112**, 13763–13768 (2008).
- Jia, G., Yang, M., Song, Y., You, H. & Zhang, H. General and facile method to prepare uniform Y₂O₃: Eu hollow microspheres. *Cryst. Growth Des.* **9**, 301–307 (2008).
- Suehiro, T., Hirotsaki, N., Xie, R.-J. & Sato, T. Blue-emitting LaSi₃N₅: Ce³⁺ fine powder phosphor for UV-converting white light-emitting diodes. *Appl. Phys. Lett.* **95**, 51903 (2009).
- Jayachandriah, C., Kumar, K. S., Krishnaiah, G. & Rao, N. M. Influence of Dy dopant on structural and photoluminescence of Dy-doped ZnO nanoparticles. *J. Alloys Compd.* **623**, 248–254 (2015).
- Zhang, Y. *et al.* A new single-phase white-light-emitting CaWO₄: Dy³⁺ phosphor: synthesis, luminescence and energy transfer. *RSC Adv.* **5**, 62527–62533 (2015).
- Liu, H. *et al.* A novel single-phase white light emitting phosphor Ca₉La(PO₄)₅(SiO₄)₂F₂: Dy³⁺: synthesis, crystal structure and luminescence properties. *RSC Adv.* **6**, 24577–24583 (2016).
- Zhang, Z. *et al.* Enhanced novel white emission in Ca₃(PO₄)₂: Dy³⁺ single-phase full-color phosphor by charge compensation. *J. Mater. Sci. Mater. Electron.* **26**, 1923–1931 (2015).
- Zhang, Z. W. *et al.* A novel white emission in Ca₈MgBi(PO₄)₇: Dy³⁺ single-phase full-color phosphor. *J. Alloys Compd.* **601**, 231–233 (2014).
- Wang, J., Wang, J. & Duan, P. Luminescent properties of Dy³⁺ doped Sr₃Y(PO₄)₃ for white LEDs. *Mater. Lett.* **107**, 96–98 (2013).
- Yu, R. *et al.* Photoluminescence Properties of Novel Host-Sensitized Y₆WO₁₂: Dy³⁺ Phosphors. *J. Am. Ceram. Soc.* **97**, 2170–2176 (2014).
- Do Han, S., Khatkar, S. P., Taxak, V. B., Sharma, G. & Kumar, D. Synthesis, luminescence and effect of heat treatment on the properties of Dy³⁺-doped YVO₄ phosphor. *Mater. Sci. Eng. B* **129**, 126–130 (2006).
- Dutta, S., Som, S. & Sharma, S. K. Luminescence and photometric characterization of K⁺ compensated CaMoO₄: Dy³⁺ nanophosphors. *Dalt. Trans.* **42**, 9654–9661 (2013).
- Zhu, G., Ci, Z., Xin, S., Wen, Y. & Wang, Y. Warm white light generation from Dy³⁺ doped NaSr₂Nb₅O₁₅ for white LEDs. *Mater. Lett.* **91**, 304–306 (2013).
- You, P. *et al.* Luminescence properties of Dy³⁺-doped Li₂SrSiO₄ for NUV-excited white LEDs. *Opt. Mater. (Amst)*. **33**, 1808–1812 (2011).
- Zhang, X. *et al.* Luminescence properties of Ca₃Si₂O₇: Dy³⁺ phosphor for white light-emitting diodes. *Mater. Lett.* **79**, 292–295 (2012).
- Zhao, W., An, S., Fan, B. & Li, S. Tunable single-phased white-emitting phosphors Na₃YSi₃O₉: Tm³⁺, Dy³⁺. *J. Lumin.* **143**, 71–74 (2013).
- Ci, Z. *et al.* Warm white light generation from a single phase Dy³⁺ doped Mg₂Al₄Si₅O₁₈ phosphor for white UV-LEDs. *Phys. Chem. Chem. Phys.* **16**, 11597–11602 (2014).
- Reddy, G. V. L., Moorthy, L. R., Jamalajah, B. C. & Sasikala, T. Preparation, structural and luminescent properties of YAl₃(BO₃)₄: Dy³⁺ phosphor for white light-emission under UV excitation. *Ceram. Int.* **39**, 2675–2682 (2013).
- Dillip, G. R., Dhoble, S. J. & Raju, B. D. P. Luminescence properties of Na₃Sr₅O₁₀: Dy³⁺ plate-like microstructures for solid state lighting applications. *Opt. Mater. (Amst)*. **35**, 2261–2266 (2013).
- Zimer, H., Albers, K. & Wittrock, U. Grazing-incidence YVO₄–Nd: YVO₄ composite thin slab laser with low thermo-optic aberrations. *Opt. Lett.* **29**, (2761–2763) (2004).
- Xu, Z. *et al.* Ln³⁺ (Ln = Eu, Dy, Sm, and Er) ion-doped YVO₄ nano/microcrystals with multiform morphologies: Hydrothermal synthesis, growing mechanism, and luminescent properties. *Inorg. Chem.* **49**, 6706–6715 (2010).
- Martinez-Huerta, M. V. *et al.* Nature of the vanadia–ceria interface in V₅+CeO₂ catalysts and its relevance for the solid-state reaction toward CeVO₄ and catalytic properties. *J. Catal.* **225**, 240–248 (2004).
- Huignard, A., Gacoin, T. & Boilot, J.-P. Synthesis and luminescence properties of colloidal YVO₄: Eu phosphors. *Chem. Mater.* **12**, 1090–1094 (2000).
- Li, G., Chao, K., Peng, H. & Chen, K. Hydrothermal synthesis and characterization of YVO₄ and YVO₄: Eu³⁺ nanobelts and polyhedral micron crystals. *J. Phys. Chem. C* **112**, 6228–6231 (2008).
- Fields, R. A., Birnbaum, M. & Fincher, C. L. Highly efficient Nd: YVO₄ diode-laser end-pumped laser. *Appl. Phys. Lett.* **51**, 1885–1886 (1987).
- Huignard, A., Buissette, V., Franville, A.-C., Gacoin, T. & Boilot, J.-P. Emission Processes in YVO₄:Eu Nanoparticles. *J. Phys. Chem. B* **107**, 6754–6759 (2003).
- Wang, H., Odawara, O. & Wada, H. Morphology and optical properties of YVO₄: Eu³⁺ nanoparticles fabricated by laser ablation in ethanol. *Appl. Surf. Sci.* **425**, 689–695 (2017).
- Dolinskaya, Y. A. *et al.* Sol-gel synthesis and luminescent properties of YVO₄: Eu nanoparticles. *Glas. Phys. Chem.* **39**, 308–310 (2013).
- Riwotzki, K. & Haase, M. Colloidal YVO₄: Eu and YPO₄: 95V₀. 05O₄: Eu nanoparticles: luminescence and energy transfer processes. *J. Phys. Chem. B* **105**, 12709–12713 (2001).
- Kolesnikov, I. E. *et al.* Concentration effect on structural and luminescent properties of YVO₄:Nd³⁺ nanophosphors. *Mater. Res. Bull.* **70**, 799–803 (2015).
- Thakur, S. & Gathania, A. K. Synthesis and characterization of YVO₄-based phosphor doped with Eu³⁺ ions for display devices. *J. Electron. Mater.* **44**, 3444–3449 (2015).
- Qi, W., Chen, G., Yang, C., Luo, C. & Zhao, X. Facile hydrothermal synthesis for size-controlled YVO₄: Eu³⁺ micro/nanosheets and its luminescence properties. *J. Mater. Sci. Mater. Electron.* **28**, 9237–9244 (2017).
- Senapati, S. & Nanda, K. K. Ultrahigh-sensitive optical temperature sensing based on quasi-thermalized green emissions from Er: ZnO. *Phys. Chem. Chem. Phys.* **19**, 2346–2352 (2017).
- Vetrone, F. *et al.* Temperature sensing using fluorescent nanothermometers. *ACS Nano* **4**, 3254–3258 (2010).
- Wawrzynczyk, D., Bednarkiewicz, A., Nyk, M., Strek, W. & Samoc, M. Neodymium(iii) doped fluoride nanoparticles as non-contact optical temperature sensors. *Nanoscale* **4**, 6959 (2012).
- Chen, B. *et al.* Amphiphilic silane modified NaYF₄: Yb, Er loaded with Eu (TTA) ₃ (TPPO) ₂ nanoparticles and their multi-functions: dual mode temperature sensing and cell imaging. *Nanoscale* **5**, 8541–8549 (2013).
- Dong, B. *et al.* Temperature sensing and *in vivo* imaging by molybdenum sensitized visible upconversion luminescence of rare-earth oxides. *Adv. Mater.* **24**, 1987–1993 (2012).

40. Mahia, J. *et al.* Influence of Calcination Temperature on Lattice Parameters and Particle Size of R₂CuO₄ Compounds (R=Gd, Nd) Prepared by a Sol-Gel Method. *J. Solid State Chem.* **122**, 25–30 (1996).
41. Zhu, L. *et al.* Sonochemical synthesis and photoluminescent property of YVO₄:Eu nanocrystals. *Nanotechnology* **18**, (55604) (2007).
42. Kim, M. & Kang, S. Processing effect on the luminescence and raman spectra of Gd^{1-x}VO₄:Eu^x phosphors. *J. Mater. Res.* **22**, 2288–2296 (2007).
43. Sanson, A. *et al.* Vibrational dynamics of single-crystal YVO₄ studied by polarized micro-Raman spectroscopy and ab initio calculations. *Phys. Rev. B* **86**, 214305 (2012).
44. Yu, M., Lin, J., Fu, J. & Han, Y. C. Sol-gel fabrication, patterning and photoluminescent properties of LaPO₄:Ce³⁺, Tb³⁺ nanocrystalline thin films. *Chem. Phys. Lett.* **371**, 178–183 (2003).
45. Hsu, C. & Powell, R. C. Energy transfer in europium doped yttrium vanadate crystals. *J. Lumin.* **10**, 273–293 (1975).
46. Kuang, J., Liu, Y. & Zhang, J. White-light-emitting long-lasting phosphorescence in Dy³⁺-doped SrSiO₃. *J. Solid State Chem.* **179**, 266–269 (2006).
47. Babu, P. *et al.* Spectral investigations on Dy³⁺-doped transparent oxyfluoride glasses and nanocrystalline glass ceramics. *J. Appl. Phys.* **105**, 13516 (2009).
48. Dolinskaya, Y. A. *et al.* Sol-gel synthesis and luminescent properties of YVO₄:Eu nanoparticles. *Glas. Phys. Chem.* **39**, 308–310 (2013).
49. Kang, Y. C., Lenggoro, I. W., Park, S. B. & Okuyama, K. YAG:Ce phosphor particles prepared by ultrasonic spray pyrolysis. *Mater. Res. Bull.* **35**, 789–798 (2000).
50. Kumar, A., Babu, S., Karakoti, A. S., Schulte, A. & Seal, S. Luminescence properties of europium-doped cerium oxide nanoparticles: role of vacancy and oxidation states. *Langmuir* **25**, 10998–11007 (2009).
51. Zhang, H., Fu, X., Niu, S., Sun, G. & Xin, Q. Low temperature synthesis of nanocrystalline YVO₄:Eu via polyacrylamide gel method. *J. Solid State Chem.* **177**, 2649–2654 (2004).
52. Yang, E. *et al.* Kinetic Control over YVO₄:Eu³⁺ Nanoparticles for Tailored Structure and Luminescence Properties. *J. Phys. Chem. C* **118**, 3820–3827 (2014).
53. Wiglusz, R. J. Bednarkiewicz, A. & Streck, W. Role of the sintering temperature and doping level in the structural and spectral properties of Eu-doped nanocrystalline YVO₄. *Inorg. Chem.* **51**, 1180–1186 (2011).
54. Kolesnikov, I. E., Mamonova, D. V., Lähderanta, E., Kurochkin, A. V. & Mikhailov, M. D. The impact of doping concentration on structure and photoluminescence of Lu₂O₃:Eu³⁺ nanocrystals. *J. Lumin.* **187**, (26–32) (2017).
55. Kolesnikov, I. E. *et al.* Concentration effect on photoluminescence of Eu³⁺-doped nanocrystalline YVO₄. *J. Lumin.* **158**, 469–474 (2015).
56. Kolesnikov, I. E. *et al.* Asymmetry ratio as a parameter of Eu³⁺ local environment in phosphors. *J. Rare Earths* **36**, 474–481 (2018).
57. Oomen, E. & Van Dongen, A.-M. A. Europium (III) in oxide glasses: dependence of the emission spectrum upon glass composition. *J. Non. Cryst. Solids* **111**, 205–213 (1989).
58. Fawad, U., Kim, H. J., Khan, S., Khan, M. & Ali, L. Photoluminescent properties of white-light-emitting Li₆Y (BO₃)₃:Dy³⁺ phosphor. *Solid State Sci.* **62**, 1–5 (2016).
59. Fujii, T. *et al.* Photochromic behavior in the fluorescence spectra of 9-anthrol encapsulated in Si-Al glasses prepared by the sol-gel method. *J. Phys. Chem. B* **101**, 10631–10637 (1997).
60. Streck, W., Zych, E. & Hreniak, D. Size effects on optical properties of Lu₂O₃:Eu³⁺ nanocrystallites. *J. Alloys Compd.* **344**, (332–336) (2002).
61. Zheng, Y. *et al.* Facile hydrothermal synthesis and luminescent properties of large-scale GdVO₄:Eu³⁺ nanowires. *Cryst. Growth Des.* **9**, 5101–5107 (2009).
62. Sudarsan, V., van Veggel, F. C. J. M., Herring, R. A. & Raudsepp, M. Surface Eu³⁺ ions are different than 'bulk' Eu³⁺ ions in crystalline doped LaF₃ nanoparticles. *J. Mater. Chem.* **15**, 1332 (2005).
63. Singh, N. S., Ningthoujam, R. S., Luwang, M. N., Singh, S. D. & Vatsa, R. K. Luminescence, lifetime and quantum yield studies of YVO₄:Ln³⁺ (Ln³⁺ = Dy³⁺, Eu³⁺) nanoparticles: Concentration and annealing effects. *Chem. Phys. Lett.* **480**, 237–242 (2009).
64. Blasse, G. & Brill, A. A New Phosphor For Flying-Spot Cathode-Ray Tubes For Color Television: Yellow-Emitting Y₃Al₅O₁₂-Ce³⁺. *Appl. Phys. Lett.* **11**, 53–55 (1967).
65. Naik, R. *et al.* Low temperature synthesis and photoluminescence properties of red emitting Mg₂SiO₄:Eu³⁺ nanophosphor for near UV light emitting diodes. *Sensors Actuators B Chem.* **195**, 140–149 (2014).
66. Blasse, G. Energy transfer in oxidic phosphors. *Phys. Lett. A* **28**, 444–445 (1968).
67. Chikte, D., Omanwar, S. K. & Moharil, S. V. Luminescence properties of red emitting phosphor NaSrBO₃:Eu³⁺ prepared with novel combustion synthesis method. *J. Lumin.* **142**, 180–183 (2013).
68. Van Uitert, L. G. Characterization of Energy Transfer Interactions between Rare Earth Ions. *J. Electrochem. Soc.* **114**, 1048 (1967).
69. Ozawa, L. & Jaffe, P. M. Mechanism of Emission Color Shift with Activator Concentration in Eu³⁺ Activated Phosphors. *J. Electrochem. Soc.* **118**, 1678–1979 (1971).
70. Ozawa, L. Determination of self-concentration quenching mechanisms of rare earth luminescence from intensity measurements on powdered phosphor screen. *J. Electrochem. Soc.* **126**, 106–109 (1979).
71. Yang, F. *et al.* Sm³⁺-doped Ba₃Bi(PO₄)₃ orange reddish emitting phosphor. *Spectrochim. Acta Part A Mol. Biomol. Spectrosc.* **105**, 626–631 (2013).
72. Ximendes, E. C., Rocha, U., Kumar, K. U., Jacinto, C. & Jaque, D. LaF₃ core/shell nanoparticles for subcutaneous heating and thermal sensing in the second biological-window. *Appl. Phys. Lett.* **108**, 253103 (2016).
73. Li, L. *et al.* Visible-Light Excited Luminescent Thermometer Based on Single Lanthanide Organic Frameworks. *Adv. Funct. Mater.* **26**, 8677–8684 (2016).
74. Benayas, A. *et al.* Nd:YAG Near-Infrared Luminescent Nanothermometers. *Adv. Opt. Mater.* **3**, 687–694 (2015).
75. Marciniak, L., Bednarkiewicz, A. & Elzbiaciak, K. NIR-NIR photon avalanche based luminescent thermometry with Nd³⁺ doped nanoparticles. *J. Mater. Chem. C* **6**, 7568–7575 (2018).
76. Debasu, M. L. *et al.* All-In-One Optical Heater-Thermometer Nanoplatfrom Operative From 300 to 2000 K Based on Er³⁺ Emission and Blackbody Radiation. *Adv. Mater.* **25**, 4868–4874 (2013).
77. Bu, Y. Y., Cheng, S. J., Wang, X. F. & Yan, X. H. Optical thermometry based on luminescence behavior of Dy³⁺-doped transparent LaF₃ glass ceramics. *Appl. Phys. A* **121**, 1171–1178 (2015).
78. Kolesnikov, I. E. *et al.* New strategy for thermal sensitivity enhancement of Nd³⁺-based ratiometric luminescence thermometers. *J. Lumin.* **192**, 40–46 (2017).
79. Brites, C. D. S. *et al.* Thermometry at the nanoscale. *Nanoscale* **4**, 4799–4829 (2012).
80. Cao, Z. *et al.* Temperature dependent luminescence of Dy³⁺-doped BaYF₅ nanoparticles for optical thermometry. *Curr. Appl. Phys.* **14**, 1067–1071 (2014).
81. Čulubrk, S., Lojpur, V., Ahrenkiel, S. P., Nedeljković, J. M. & Dramićanin, M. D. Non-contact thermometry with Dy³⁺-doped Gd₂Ti₂O₇ nano-powders. *J. Lumin.* **170**, 395–400 (2016).
82. Chepyga, L. M., Osvet, A., Brabec, C. J. & Batentschuk, M. High-temperature thermographic phosphor mixture YAP/YAG:Dy³⁺ and its photoluminescence properties. *J. Lumin.* **188**, 582–588 (2017).
83. Anderson, B. R., Gunawidjaja, R. & Eilers, H. Dy³⁺-doped yttrium complex molecular crystals for two-color thermometry in heterogeneous materials. *J. Lumin.* **188**, 238–245 (2017).

Acknowledgements

This research has been funded by the Russian Science Foundation (No. 17-72-10055). Experimental measurements were performed in “Center for Optical and Laser materials research”, “Research Centre for X-ray Diffraction Studies”, “Interdisciplinary Resource Center for Nanotechnology” (St. Petersburg State University).

Author Contributions

I.E.K. wrote the main manuscript text and managed the workflow. A.A.K. performed steady state and kinetics luminescence measurements. M.A.K. carried out thermometry measurements and analyzed the data. A.S.T. and E.V.G. were responsible for sample synthesis and structural and morphology measurements. E.Yu.K. contributed during data post-processing and prepared figures. E.L. contributed with helpful ideas and improvements to be made to the manuscript’s main text and general idea. Final version of manuscript was approved by all authors.

Additional Information

Supplementary information accompanies this paper at <https://doi.org/10.1038/s41598-019-38774-6>.

Competing Interests: The authors declare no competing interests.

Publisher’s note: Springer Nature remains neutral with regard to jurisdictional claims in published maps and institutional affiliations.



Open Access This article is licensed under a Creative Commons Attribution 4.0 International License, which permits use, sharing, adaptation, distribution and reproduction in any medium or format, as long as you give appropriate credit to the original author(s) and the source, provide a link to the Creative Commons license, and indicate if changes were made. The images or other third party material in this article are included in the article’s Creative Commons license, unless indicated otherwise in a credit line to the material. If material is not included in the article’s Creative Commons license and your intended use is not permitted by statutory regulation or exceeds the permitted use, you will need to obtain permission directly from the copyright holder. To view a copy of this license, visit <http://creativecommons.org/licenses/by/4.0/>.

© The Author(s) 2019